Fire Safety Journal 140 (2023) 103859

Contents lists available at ScienceDirect

Fire Safety Journal

journal homepage: www.elsevier.com/locate/firesaf

Measuring firebrand heat flux with a thin-skin calorimeter

Amy E. Mensch *, Savannah S. Wessies, Anthony Hamins, Jiann C. Yang

National Institute of Standards and Technology, 100 Bureau Dr., Gaithersburg, 20899, MD, USA

ARTICLE INFO

Keywords:
Wildland-urban interface fires
Firebrands
Heat transfer
Thin skin calorimeter

ABSTRACT

While the impact of wildland-urban interface fires is growing, firebrand exposure is a significant but not well understood contributor to fire spread. The ignition threat of firebrand exposures can be characterized by measuring the heat transfer of glowing firebrands to a surface. The current study presents a novel method for conducting time-resolved heat transfer measurements from individual firebrands across a range of flow conditions. Experiments are conducted with individual glowing firebrands generated from birch discs and placed on a copper thin skin calorimeter of the same diameter, which is embedded in the substrate. The net heat flux from the firebrand to the thin skin calorimeter is obtained from the thermal energy storage in the thin skin calorimeter, plus heat conduction losses to the substrate. Values of peak net heat flux, total heating, duration of heating are reported under different flow conditions from 0.05 m/s to 1.6 m/s. The average peak net heat flux for the disc-shaped birch firebrands is 45 kW/m^2, and does not change significantly with flow condition. However, there is an increase in the total heating, duration of heating, and total mass consumed as the flow velocity increases.

1. Introduction

Fire losses in communities within and bordering wildlands are a growing international problem [1]. Wildland fires that spread into communities, known as wildland-urban interface (WUI) fires, can lead to substantial life and property loss. These fires can produce hazardous conditions that can be very difficult to control, due to the influence of topography, vegetative fuel types and distribution, local weather conditions, such as low humidity and high winds. Of the 10 costliest wildland fires in the USA, seven have occurred since 2000 [2]. In the last 10 years in California alone, one of every eight acres of land has burned, over 43,000 structures have been destroyed, and 173 lives have been lost [3]. The 2018 and 2020 Northern California wildfire incidents referred to as the “Camp Fire" and the “2020 Fire Siege” caused 116 fatalities including 3 firefighters, destroyed over 28,000 structures with an estimated costs of about $15 B (in 2021 U.S. dollars) [3–5]. In Australia, 173 people lost their lives and more than 3500 buildings were destroyed in the 2009 Victoria Black Saturday fires [6]. In Portugal, the year 2017 witnessed the highest on record of total burned area since 1980 (above half a million hectares), 115 fatalities and activation of about 1500 firefighters to address the WUI fires [7].

Firebrands have been identified as playing a key role in fire spread and ignition of structural components during WUI fires and are thought to cause as many as 90% of structural ignitions during wildfire incidents [8]. Fire spread by firebrands involves a set of serial processes, beginning with firebrand production, firebrand transport, and firebrand deposition on a substrate (such as a structural component). During transport, cellulosic brands are typically burning in a glowing rather than a flaming state. Upon landing, if the firebrand is still burning and has sufficient unburned mass, then ignition of a substrate may occur, depending on the amount of heat transfer to the substrate [9].

Nazare et al. [10] and Rein [11] present comprehensive reviews of the technical literature on firebrand research. There are several common criteria regarding ignition of a substrate. The most widely used criterion for ignition of wood is the critical ignition temperature, followed by the critical heat flux for ignition, and the critical mass loss rate of the target fuel. These critical ignition criteria are usually determined through exposure to radiant heating and a pilot. Ohlemiller and Villa [12] discusses the critical ignition temperature for both thermally thick and thermally thin target fuels. For all three critical ignition criteria, the ignition is driven by heat transfer from the heat source (firebrand) to a substrate, which is the subject of this study.

Ignition by firebrands is a transient phenomenon involving heat transfer from the firebrand to the fuel. Even a single brand can ignite a cellulosic fuel bed [13]. As compared to radiative heat sources, conductive heat sources can initiate smoldering fires with a much lower heat flux [11]. The likelihood of a single firebrand to cause ignition of

* Corresponding author.
E-mail addresses: amy.mensch@nist.gov (A.E. Mensch), savannah.wessies@nist.gov (S.S. Wessies), anthony.hamins@nist.gov (A. Hamins), jiann.yang@nist.gov (J.C. Yang).

https://doi.org/10.1016/j.firesaf.2023.103859
Received 5 June 2023; Accepted 4 July 2023
Available online 11 July 2023
0379-7112/Published by Elsevier Ltd.

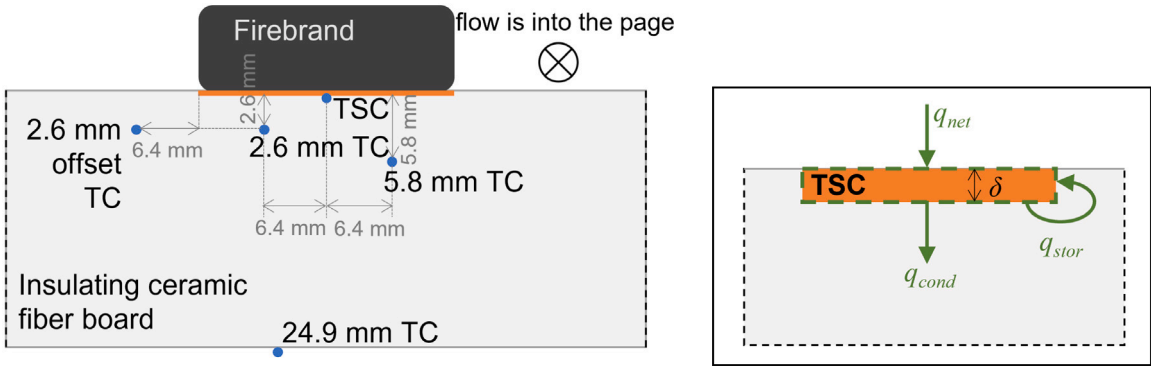

Fig. 1. Diagrams of (a) the TSC system and thermocouple locations and (b) the thermal energy balance on the TSC.

a non-porous combustible solid may be limited by the thermal mass of the substrate compared to the heating from the firebrand. Various studies report different critical heat flux values for glowing ignition in wood specimens, depending on the experimental conditions (such as convective flow) and the duration of the test [9].

To help develop fire-resistant WUI communities and protect structures from ignition, it is imperative to quantify the exposure threat posed by firebrands to structures and structural materials. Only after the structural ignition threat is fully understood can cost-effective and appropriate technological solutions be developed. Measurements of the time-dependent heat flux from a single firebrand on a substrate is an essential step towards a fundamental understanding of substrate ignition by firebrands. This paper presents a method to use a thin skin calorimeter (TSC) to quantify the thermal hazard of individual well characterized firebrands over a range of flow conditions.

1.1. Previous measurements

Most previous experimental work on firebrand ignition has been mainly phenomenological, delivering firebrands onto various combustible materials and geometries and reporting observations on the likelihood of ignition. Few investigations have explored the mechanism of ignition through measurements of the heat flux from firebrands or firebrand piles. The methods used to measure heat flux in these investigations are summarized below.

Hakes et al. [14] and Richter et al. [15] used a water-cooled heat flux gauge to measure the heat flux from cylindrical firebrands to a substrate. Thomas et al. [16] determined the net heat flux from firebrand piles to an inert solid substrate with an inverse heat transfer model using temperatures measured within the substrate. The net heat flux was lower than the heat flux measured by a water-cooled heat flux gauge at the surface of the substrate, which the authors attributed to differences in accounting for heat losses. Bearinger et al. [17] also used an inverse heat transfer analysis to determine the heat flux from individual smoldering firebrands. Infrared thermography on the underside of the substrate allowed them to report spatial distributions of heat flux with a resolution of 0.4 mm. A thin skin calorimeter, defined in ASTM E469, is typically used for quantifying radiant heat flux in fire experiments [18], but can also be used to measure heat flux to a surface. Hakes et al. [14] used an array of thin skin calorimeters to understand the spatial distribution of heat flux on a substrate from deposited firebrands under ambient conditions, but the authors only reported heat flux under wind conditions measured by their water-cooled heat flux gauge. Across all measurement methods, individual firebrand peak net heat fluxes have ranged between 10 kW/m^2 and 30 kW/m^2 (over the firebrand initial projected area), for cylindrical or rod-shaped firebrands and for wind conditions between no flow and 2 m/s [14,17].

Table 1
Thermal properties.

	TSC	Substrate
Material	copper	ceramic fiber board
c_p (kJ/kg K)	0.385	1.089
ρ (kg/m^3)	8960	336
k (W/m K)	392	0.068

2. Methods

2.1. Experimental setup

Heat transfer measurements from an individual firebrand to a substrate were conducted using a TSC. The TSC heat flux measurement was based on the rate of change in the temperature of a metal disc, referred to as the TSC. The TSC was made from copper with a thickness, δ, of 0.552 mm and a diameter, D, of 25.4 mm. The Biot number of the TSC was estimated to be much less than unity, on the order of 10^{-5} based on δ and on the order of 10^{-3} based on D, allowing the assumption of a uniform temperature throughout the TSC. The TSC was embedded flush with the surface of a 25.4 mm thick insulating substrate made of ceramic fiber board as shown in Fig. 1. The thermophysical properties of the TSC and substrate are given in Table 1, where c_p is specific heat, ρ is density, and k is thermal conductivity.

For measuring the TSC temperature, the wires of a K-type thermocouple (TC), 0.25 mm diameter, were welded to the unexposed surface of the TSC. The TSC temperature data were recorded at 6 Hz. Additional K-type TCs were installed at different locations within the substrate to estimate conductive heat losses from the TSC. The locations of the TCs in the substrate are shown in Fig. 1(a). Small holes, 1.5 mm to 2.4 mm in diameter, were drilled vertically from the bottom of the substrate for the TC installation.

The TSC and top surface of the substrate were flush with the floor of a single-pass wind tunnel depicted in Fig. 2. Ambient room air entered through a 406 mm by 406 mm square inlet containing a honeycomb flow straightener, after which the flow path was constricted to 305 mm by 305 mm. The glowing firebrands were placed on top of the TSC, located 1.30 m downstream from the constriction, using the door on the side of the tunnel. A quartz window on the top of the tunnel allowed visual access during the experiments. About 250 mm downstream of the TSC, the tunnel constricted again to connect to the axial blower. Four flow velocities represented different wind conditions for the firebrands. The flow velocity was measured before the experiments with a hot wire anemometer at 12.7 mm above the TSC, which was close to the height of the firebrand when placed on the TSC. The mean velocity and standard uncertainty for a 95% confidence interval for each flow condition are 1.6 m/s ± 0.09 m/s, 1.0 m/s ± 0.06 m/s, 0.6 m/s ± 0.03 m/s, and 0.05 m/s ± 0.003 m/s.

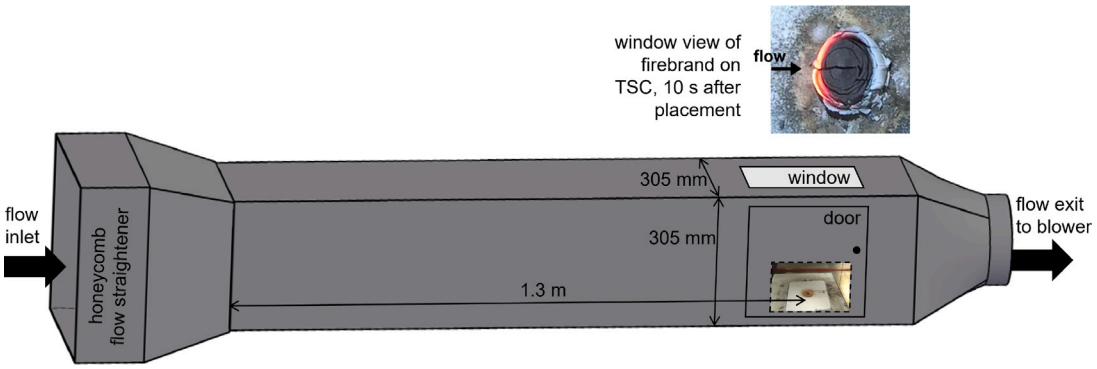

Fig. 2. Depiction of the single-pass wind tunnel to generate four flow conditions, with velocities between 0.05 m/s and 1.6 m/s. The TSC and substrate are shown behind the side door.

Glowing firebrands were generated with a repeatable procedure using birch wood discs with a diameter of 31.75 mm and a thickness of 10.6 mm, cut from commercially available dowels. Before testing, the discs were completely dried in an oven at 110 °C for more than 8 h. The dried birch discs had a mean mass of 4.95 g ± 0.11 g. The mass loss from drying was between 8% and 11% of the original mass. To generate a glowing firebrand, a dried birch disc was placed on the wire mesh base of a metal chimney, 150 mm in diameter and 180 mm tall. The chimney was positioned over a 50 mm diameter burner with a pre-lit propane flame. This exposed the birch disc to direct flame contact, which lasted for 10 s before the propane fuel was turned off. This consistent exposure time allowed for the birch discs to ignite and burn with a self-sustaining flame in the chimney. The flame was allowed to self-extinguish, which occurred an average of 246 s ± 7 s after the initial chimney placement on the propane burner. Then the glowing firebrand was picked up with tongs and placed on top of the TSC inside the wind tunnel using the side door. Placement on the TSC occurred approximately 5 s after self-extinguishment. This firebrand generation procedure typically shrank the firebrand to approximately the same diameter as the TSC (25.4 mm), by design to prevent cooling of the TSC from exposure to the surroundings. Following the experiment, the mass of remnants of the firebrand was measured. Six or seven repeated firebrand tests were conducted for each flow condition.

To evaluate the repeatability of the firebrand generation process, additional tests were conducted to measure the temperature rise of the birch discs during this procedure. A 1.59 mm diameter sheathed K-type TC was inserted into a hole of the same diameter drilled from the side to the center of the birch disc at half of the thickness. The embedded temperature profiles of four tests of the same size birch discs are shown in Fig. 3. The data begins with the start of the exposure to the propane burner flame, and the data ends when the firebrand flame self-extinguished. The temperature rise in each test is similar, and the self-extinguishment temperatures and times are consistent across tests. The average final temperature was 501 °C ± 14 °C, and the average time until self-extinguishment was 201 s ± 17 s. The time until self-extinguishment was about 20% less than the time for firebrands generated for the heat flux measurements because the birch discs with holes had about 20% less mass.

2.2. Heat flux measurements

The net heat flux from the firebrand to the TSC, q_{net}, was determined using an energy balance on the TSC, represented in Fig. 1(b) and in Eq. (1).

$$q_{net} = q_{stor} + q_{cond} = (\rho V c_p)_{TSC} \frac{dT_{TSC}}{dt} + q_{cond} \tag{1}$$

The thermal storage term, q_{stor}, was a function of the density, ρ, volume, V, and specific heat, c_p, of copper, and of the derivative of the TSC temperature with respect to time, dT_{TSC}/dt. The time derivative was computed numerically using a second order central difference. For all the experiments conducted, the peak dT_{TSC}/dt occurred between 1.0 s and 2.2 s from $t = 0$, which was defined as the time of the initial TSC temperature rise above the background temperature.

In addition to the thermal storage of the TSC, we accounted for the conductive losses from the TSC to the insulating substrate, q_{cond}, to better quantify the heat flux exposure from the firebrand, q_{net}. The firebrand was much hotter than the TSC during the experiment. Additionally, the firebrand covered the top surface of the TSC, preventing exposure to air flow. With this in mind, we assumed convective and radiative losses from the top surface of the TSC were negligible. Eq. (1) was converted to the net heat flux from the firebrand to the TSC, in Eq. (2), by dividing by the surface area of the TSC exposed to the firebrand, $A_{surf} = \pi D^2/4$.

$$q''_{net} = (\rho c_p \delta)_{TSC} \frac{dT_{TSC}}{dt} + \frac{q_{cond}}{A_{surf}} = (\rho c_p \delta)_{TSC} \frac{dT_{TSC}}{dt} + q''_{cond} \tag{2}$$

The $q''_{cond,exp}$ was determined experimentally by the TCs in the substrate. Fig. 4 provides an example of typical temperature measurements for the TSC and substrate TCs (locations shown in Fig. 1(a)). The TSC temperature was recorded at a rate of 6 Hz, and substrate temperatures were recorded at 3 Hz. The substrate temperatures slowly increased after the initial TSC temperature rise, but the 24.9 mm TC on the bottom of the substrate showed almost no increase. While the conductive heat loss may not be significant initially, $q''_{cond,exp}$ contributed to the total heating of the substrate over time.

We estimated the conductive losses from the TSC to the substrate in both the vertical and lateral directions using Fourier's Law. The TSC temperature was assumed to be uniform due to its low Biot number, and there was assumed to be no contact resistance between the TSC and the substrate, due to a snug assembly of the TSC into the substrate. Each component of conductive heat loss from the TSC was estimated using $q_{cond,exp} = -k_s A \Delta T / L$, where k_s was the thermal conductivity of the substrate, A was the heat transfer surface area, ΔT was the temperature difference, and L was the distance between the temperatures. First, we considered the vertical component using the temperatures of the TSC and the closest thermocouple, 2.6 mm TC, with A equal to A_{surf}, and the distance equal to 2.6 mm. For the lateral conduction, we considered the temperature difference between the substrate 2.6 mm below the edge of the TSC and the 2.6 mm offset TC. We assumed the temperature of the substrate 2.6 mm below the edge of the TSC was the same as the 2.6 mm TC temperature. The heat transfer surface area was equal to (πD x 2.6 mm) and the perpendicular distance from the edge of the TSC was equal to 6.4 mm. The vertical and lateral portions of the heat transfer were summed to determine the total conductive losses from the TSC, before dividing by A_{surf} to obtain $q''_{cond,exp}$.

The uncertainty in the peak q''_{net} was estimated to be ± 15% to ± 20%, based on estimates of the uncertainty in δ, dT_{TSC}/dt, and $q''_{cond,exp}$. A coverage factor of 2 was included after the individual

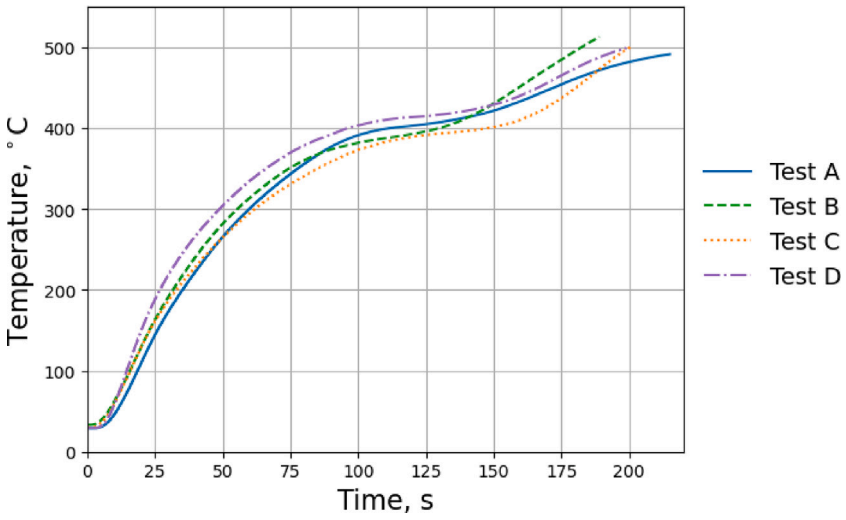

Fig. 3. Temperature measured by the sheathed thermocouple inside the birch wood disc during the firebrand generation procedure for four repeat tests.

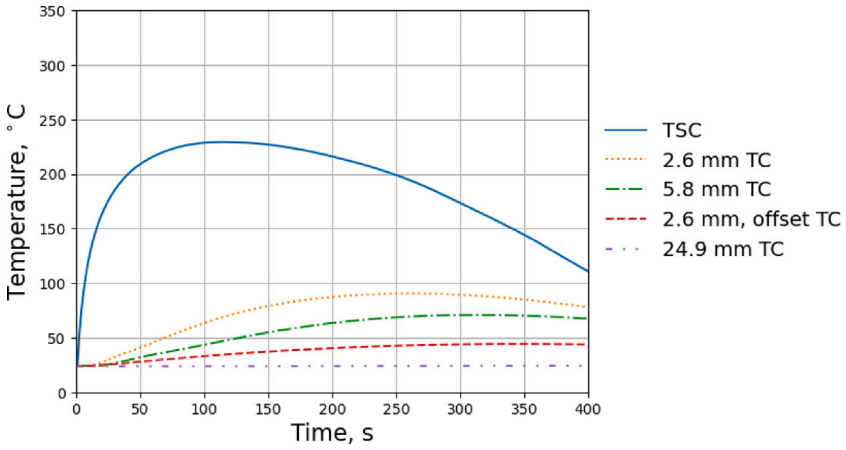

Fig. 4. Evolution of temperatures measured within the TSC and substrate system at the locations shown in Fig. 1(a) during an experiment with the 1.0 m/s flow condition.

Table 2
Contributions to uncertainty in peak q''_{net} from the uncertainties in δ, dT_{TSC}/dt, and $q''_{cond,exp}$, with a coverage factor of 2 used for the combined uncertainty, for two representative experiments at 0.05 m/s and 1.6 m/s.

Flow Condition	Uncert. contribution due to:			2 × Comb. Uncert.
(m/s)	δ (%)	dT_{TSC}/dt (%)	$q''_{cond,exp}$ (%)	(%)
1.6	1.2	9.8	0.2	20
0.05	1.2	7.4	0.2	15

uncertainties were combined. The numerical calculation of dT_{TSC}/dt during the initial temperature rise had the most significant contribution to the uncertainty in q''_{net}, as shown in Table 2. The uncertainty of dT_{TSC}/dt was estimated from the change resulting from the use of a different numerical method, a first order backward difference. The uncertainty in δ was estimated from the variation in the measured thickness at different locations on the TSC, and the uncertainty in $q''_{cond,exp}$ was determined based on a 2.2 °C uncertainty in the embedded TC measurements, as reported by the manufacturer of the TC wire.

3. Results and discussion

Photos of the smoldering firebrand in the first three minutes from placement on the TSC are shown in Fig. 5 for two repeat experiments with the 1.0 m/s flow condition. Initially, glowing is observed around the circumference of the firebrand, surrounded by ash where the wood has previously burned. Within 30 s, the glowing is concentrated toward the leading edge of the firebrand, where the incoming flow supports the smoldering reaction. At 90 s, the smoldering has progressed somewhat toward the center of the firebrand, but the intensity of glowing is beginning to decrease. This time roughly corresponds with the peak temperature of the TSC in Fig. 4, after which smoldering continues to decrease and the TSC temperature begins to fall. In Test 2, the glowing is further concentrated at the large crack that happens to bisect the firebrand, demonstrating the importance of access to oxygen to sustain smoldering. In both experiments, we can observe shrinkage of the firebrand leading edge, as ash is removed by the incoming flow. In the following sections, quantitative results will be presented for all flow conditions, including TSC temperature and thermal storage, conductive losses from the TSC, net heat flux, and total heating from the firebrand.

3.1. TSC temperature and thermal storage

The TSC temperature and thermal energy storage per unit area, q''_{stor}, averaged for each flow condition, are presented in Fig. 6 for the first 60 s of heating from the firebrand. There appears to be a minor temperature effect with flow condition. At 60 s, the higher two flow conditions (Figs. 6(a) and 6(b)) exceed 200 °C, while the lower two flow conditions (Figs. 6(c) and 6(d)) are just under 200 °C. By examining the maximum TSC temperature, we can better explore this

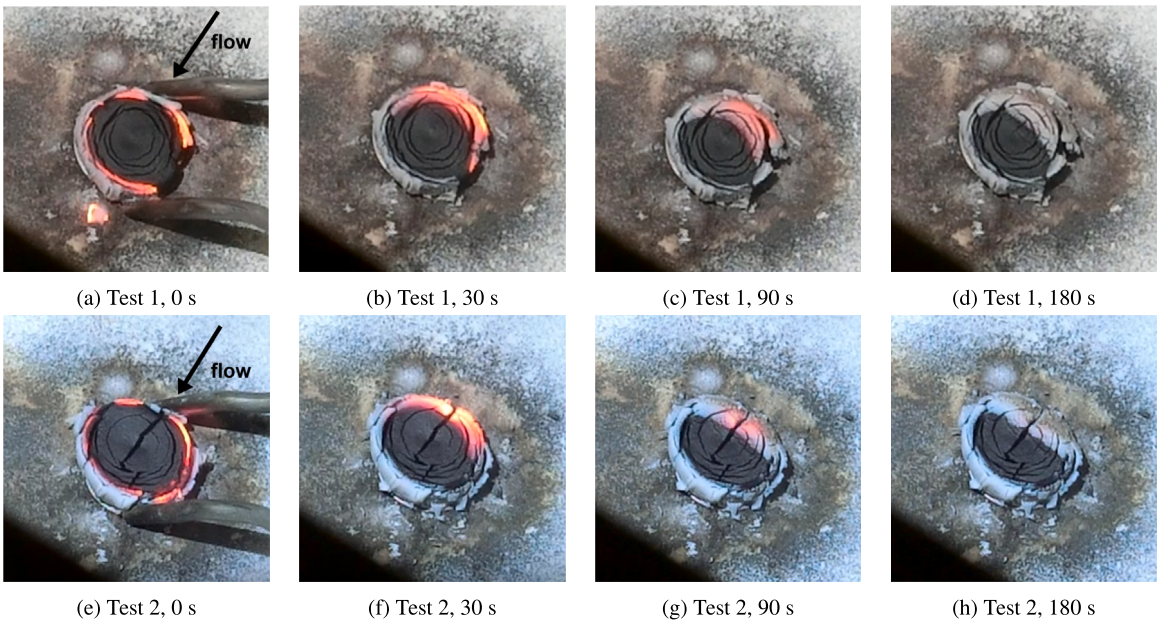

(a) Test 1, 0 s (b) Test 1, 30 s (c) Test 1, 90 s (d) Test 1, 180 s

(e) Test 2, 0 s (f) Test 2, 30 s (g) Test 2, 90 s (h) Test 2, 180 s

Fig. 5. Photos showing the progression of the firebrand from placement on the TSC during two experiments under the 1.0 m/s flow condition. Temperatures from Test 2 are shown in Fig. 4.

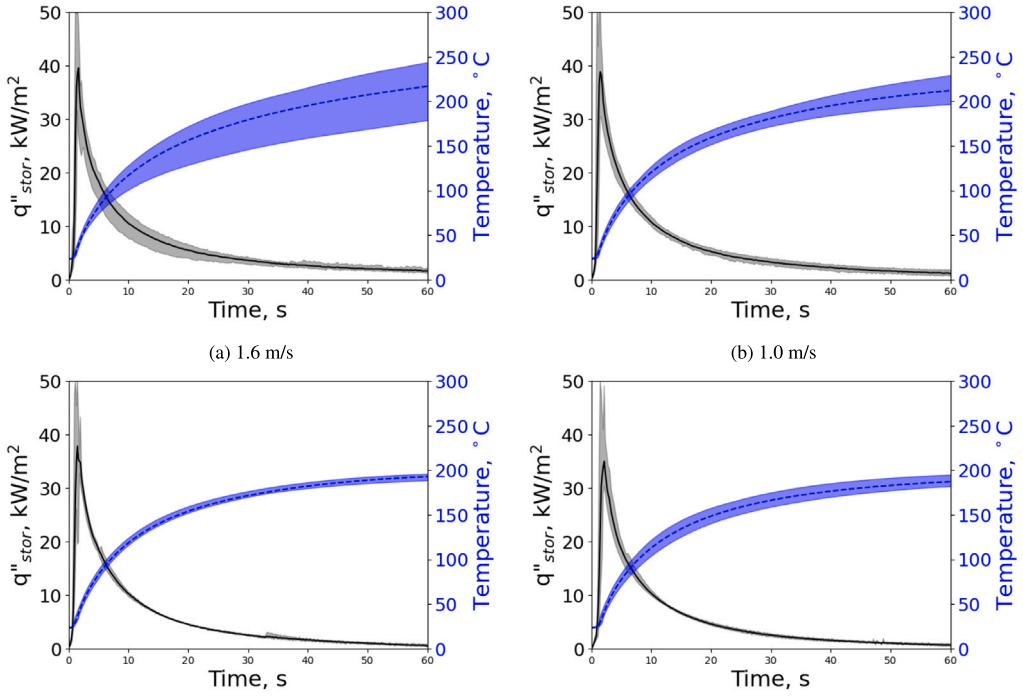

(a) 1.6 m/s (b) 1.0 m/s

(c) 0.6 m/s (d) 0.05 m/s

Fig. 6. Comparison of the TSC temperature (dashed) and thermal storage per unit area (solid) for the different flow conditions. The shaded regions represent the spread of the data between the maximum and minimum recorded at each time step among the repeat tests. There were six repeats for (a) and (c), and seven repeats for (b) and (d).

trend. The peak TSC temperature is averaged for each flow condition and reported below with the 95% confidence interval student's t-distribution. For the highest flow condition (1.6 m/s), the peak TSC temperature is 242 °C ± 20 °C over six tests. For the 1.0 m/s flow condition, averaged over seven tests, the peak temperature is 230 °C ± 19 °C. For the lower two flow conditions (0.57 m/s and 0.05 m/s), the peak temperatures are 196 °C ± 3 °C and 193 °C ± 5 °C, averaged over six and seven tests, respectively. From this analysis, we can see that there is a difference between the higher two flow conditions compared to the lower two flow conditions. However, there is not a marked difference between the peak temperatures of the two higher flow cases. Similarly, the average peak temperatures of the lower two flow conditions are within the uncertainty of one another. Although, we see some variation in the peak temperature with flow condition, there is not a similar variation in the q''_{stor} results, which are based on the change in TSC temperature with time. From the plots in Fig. 6, the initial change in temperature with time is similar for all flow conditions, leading to similar q''_{stor} results.

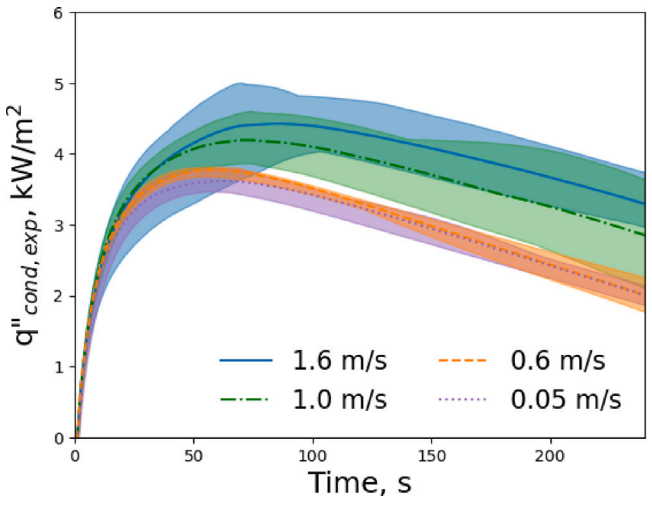

Fig. 7. Average conductive heat flux from the TSC to the substrate for the different flow conditions. The shaded regions represent the maximum and minimum $q''_{cond,exp}$ values for a given time step.

Table 3
Average peak conductive heat flux for the different flow conditions determined from experimental temperature, $q''_{cond,exp}$, and from semi-infinite analysis, $q''_{cond,theory}$. Uncertainties are based on the uncertainty of the mean value using the 95% confidence interval student's t-distribution.

Flow condition	$q''_{cond,exp}$, kW/m^2	$q''_{cond,theory}$, kW/m^2
1.6 m/s	4.5 ± 0.4	3.4 ± 0.4
1.0 m/s	4.2 ± 0.3	3.5 ± 0.2
0.6 m/s	3.8 ± 0.1	3.4 ± 0.1
0.05 m/s	3.6 ± 0.1	3.3 ± 0.2

3.2. Conductive losses

The total conductive heat fluxes from the TSC to the substrate, $q''_{cond,exp}$, averaged for the four different flow conditions, are presented in Fig. 7. At time zero, the TSC and the substrate are in thermal equilibrium, and $q''_{cond,exp}$ is zero. After firebrand deposition, the TSC temperature increases, and conductive heat loss from the TSC to the substrate begins. The initial $q''_{cond,exp}$ profiles are very similar under the four flow conditions. However, the effect of flow condition on the profiles becomes apparent as the peak $q''_{cond,exp}$ is reached. The two higher flow conditions peak at later times and at higher heat fluxes, and maintain an elevated heat flux compared to the two lower flow conditions for the remainder of the test. There is also more variation in the higher flow condition cases. The average peak conductive heat fluxes for the four flow conditions are found in Table 3.

At shorter times, when lateral conduction losses are negligible, we can also estimate the conduction losses from the TSC using 1-dimensional semi-infinite analysis. In this scenario, the TSC acts as a time varying heat flux into the semi-infinite substrate. The temperature distribution in the semi-infinite substrate with a varying heat flux at the boundary can be found in [19] and is shown in Eq. (3). In this equation, $T_s(x,t)$ is the temperature of the substrate as a function of distance from the TSC, x, and time, t, T_0 is the initial temperature of the substrate, k_s, is the thermal conductivity of the substrate, α_s is the thermal diffusivity of the substrate, q''_{cond} is the heat flux from the TSC, and τ is a dummy integration variable. Assuming perfect thermal contact at the interface between the TSC and the substrate, the TSC temperature is the same as the substrate temperature at the interface $T_s(0,t)$. This allows us to simplify Eq. (3) to determine the conductive loss term based on T_{TSC}, as seen in Eq. (4). Recognizing the convolution integral and taking a Laplace transform, we find that q''_{cond} can be calculated using Eq. (5).

$$T_s(x,t) = T_0 + \frac{1}{k_s}\left(\frac{\alpha_s}{\pi}\right)^{1/2}\int_0^t \frac{q''_{cond}(t-\tau)}{\sqrt{\tau}} exp\left(-\frac{x^2}{4\alpha_s t}\right) d\tau \quad (3)$$

$$T_{TSC}(t) = T_0 + \frac{1}{k_s}\left(\frac{\alpha_s}{\pi}\right)^{1/2}\int_0^t \frac{q''_{cond}(t-\tau)}{\sqrt{\tau}} d\tau \quad (4)$$

$$q''_{cond}(t) = \sqrt{\frac{(k\rho c_p)_s}{\pi}}\int_0^t \frac{dT_{TSC}}{dt}\bigg|_{t=\tau}\frac{1}{\sqrt{t-\tau}} d\tau \quad (5)$$

Using the semi-infinite analysis described above, the theoretical conductive losses from the TSC can be calculated using the measured TSC temperatures and are compared to the experimentally determined conduction losses described in Section 3.2 in Table 3. The conductive loss results from theory and experiments from two representative tests at the 1.0 m/s and 0.05 m/s flow conditions are presented in Fig. 8. From these two cases, we can see that the theoretical calculation, $q''_{cond,theory}$, peaks more quickly than the experimental calculation, $q''_{cond,exp}$. Additionally, the theoretical peak is lower than the experimentally determined peak. This is more evident at the higher flow cases compared to the lower flow cases, but these trends were consistent across all tests and flow conditions. The average peak $q''_{cond,theory}$ did not vary significantly with flow condition. Similarly, we did not see large discrepancies in the time to peak $q''_{cond,theory}$ for different flow conditions. Time to peak $q''_{cond,theory}$ ranged between 8.2 s and 12.2 s for all the tested conditions. These times to peak were considerably faster than the time to peak $q''_{cond,exp}$, which did show an effect of flow condition. For 1.6 m/s, times to peak $q''_{cond,exp}$ ranged between 69.5 s and 111 s. For 1.0 m/s, the range was between 68.3 s and 93.8 s. The times to peak were between 54.2 s and 63.3 s for 0.6 m/s. For 0.05 m/s the times to peak $q''_{cond,exp}$ fell between 53.8 s and 69.2 s. The $q''_{cond,exp}$ calculation may be delayed because the analysis assumes a quasi steady-state condition between the TSC and the 2.6 mm TC at each time step. However, the $q''_{cond,theory}$ peak may occur too early due to the assumption of perfect thermal contact between the TSC and substrate. Despite the differences in timing, the $q''_{cond,theory}$ and $q''_{cond,exp}$ are of similar magnitude, and the peak values are actually not significant compared to the uncertainty in the peak q''_{stor}, but are significant in the net heat flux over time. The semi-infinite model is based on the assumption of one dimensional heat transfer. At short times, when the amount of lateral heat transfer is low, the semi-infinite approximation is reasonable. However, as time progresses and lateral heat conduction becomes important, the one dimensional semi-infinite assumption of $q''_{cond,theory}$ may not be valid. From Fig. 4, we can observe that by 50 s the 2.6 mm, offset TC is increasing, and lateral conduction is occurring. In subsequent discussion, only $q''_{cond,exp}$ is used.

3.3. Peak heat flux and total heating

As shown in Sections 3.1 and 3.2, the storage and conduction losses from the TSC can be determined from the temperature history of the TSC and thermocouples embedded in the substrate. Summing these values, as shown in Eq. (2), the net heat flux from firebrand to the TSC can be determined, regardless of whether the mechanism is via conduction, radiation, or convection. Fig. 9 depicts the temporal histories of the storage and conduction components along with the net heat flux for a single test at 1.0 m/s. At short times, the net heat flux is dominated by the thermal storage in the TSC. As time progresses, the thermal storage rapidly decreases, and the conductive loss increases and becomes the dominant contribution to the net heat flux. Eventually, around 125 s, the thermal storage term becomes negative, meaning that the TSC is beginning to cool. The TSC temperature is still elevated compared to the substrate, so the conductive loss from the TSC to the substrate remains significant and slowly decays over time. The trends in the storage, conduction, and net heat flux were observed across all tests and flow conditions. There was some variation between tests in the time

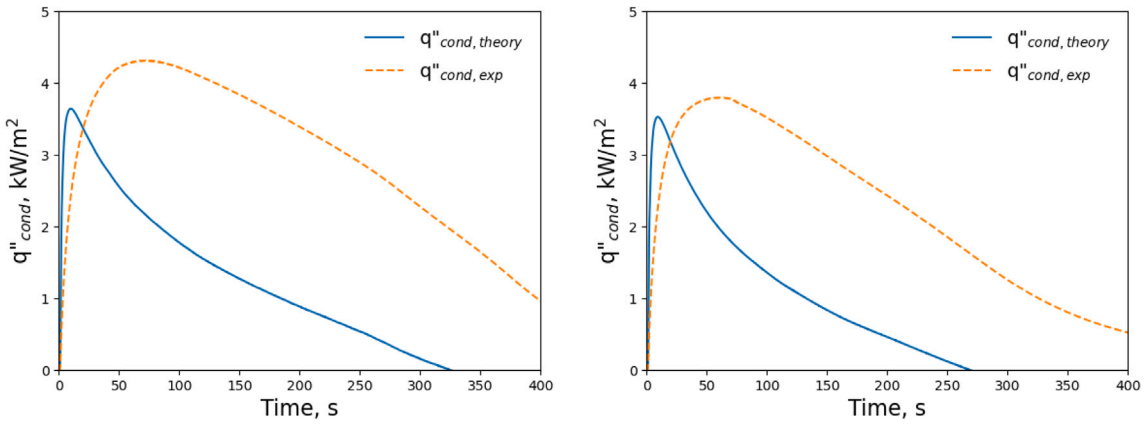

Fig. 8. Comparison of two different methods to determine the q''_{cond} loss from the TSC to the substrate for a single representative test under two different air flow conditions: (a) 1.0 m/s (same test as in Figs. 4 and 5(e)–5(h)) and (b) 0.05 m/s. $q''_{cond,theory}$ represents conduction losses calculated using the theoretical, semi-infinite analysis. $q''_{cond,exp}$ represents conduction losses determined from the experimentally measured temperatures within the substrate.

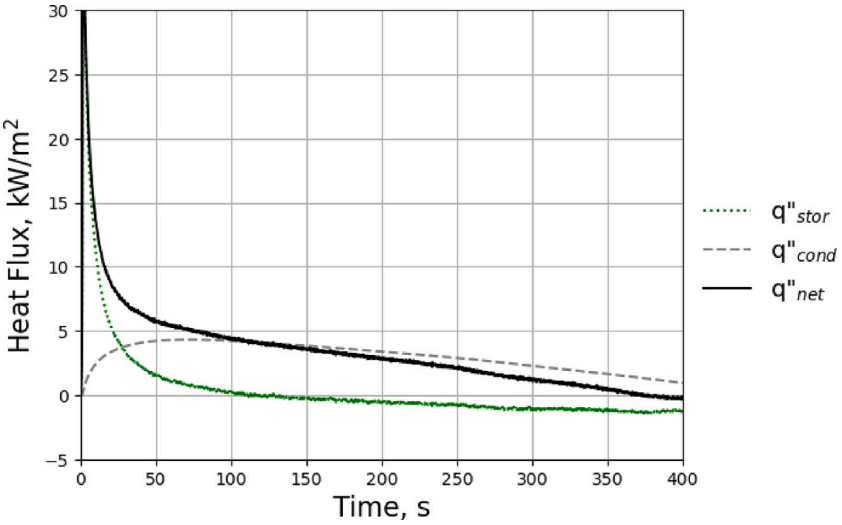

Fig. 9. Net heat flux, q''_{net}, compared to the thermal storage, q''_{stor}, and experimentally measured conduction loss, q''_{cond}, for a single representative experiment at 1.0 m/s, also shown in Figs. 4, 5(e)–5(h), and 8(a).

period before the thermal storage had a negative effect on the net heat flux. Overall, shape and magnitude of the net heat flux profiles were similar to the single firebrand net heat flux profile reported by Hakes et al. [14] for cylindrical firebrands using a water-cooled heat flux gauge. Much of the previous work in the literature reporting net heat flux profiles utilizes firebrand piles rather than individual firebrands. There are some similarities in the heat flux, although the magnitudes and time scales vary. For instance, Tao et al. [20] observed initial peak heat fluxes that quickly decayed to a relative plateau for firebrand piles placed on a water cooled heat flux gauge. Similarly, the water cooled heat flux gauge profiles for firebrand piles measured by Richter et al. [15] were characterized by a quick peak heat flux followed by a sharp decay and a period of more gradual decrease in the measured heat flux.

The peak heat flux from the net heat flux profiles can provide a measure of the hazard associated with firebrand deposition. The average peak heat flux across all tests and flow conditions was 45 kW/m^2, and on average this peak would occur after 1.6 s. As discussed in Section 2.2, the measurement uncertainty in peak q''_{net} was estimated as ± 15% to ± 20%. Due to the firebrand covering the full surface of the TSC, the reported heat flux is the area-averaged heat flux based on the contact area with the TSC. For comparison, Bearinger et al. [17], using inverse heat transfer analysis and IR thermography to measure the temperature of the back side of the substrate, reported peak heat fluxes averaged over the firebrand surface between 13.8 kW/m^2 and 27.1 kW/m^2 for their rod-shaped individual firebrands. They recorded much higher local heat flux values between 28.1 kW/m^2 and 105.8 kW/m^2.

For the different flow conditions, the average peak heat fluxes can be found in Table 4. From this table we can see that 0.05 m/s had the lowest peak flux and the highest uncertainty in the mean value. The three higher flow conditions had higher peak heat fluxes comparatively. However the peak heat fluxes from all flow conditions were within the uncertainties of each other, so there is no clear difference with flow condition.

From Table 4, the peak heat fluxes occur within seconds of deposition. At short times, the majority contribution to the net heat flux comes from the thermal storage term. In the first few seconds, the amount of conduction loss from the bottom surface of the TSC is very low, so it could be feasible to use the 1-D semi-infinite analysis for the conduction loss term. Calculating the conduction loss term with the semi-infinite analysis, the peak net heat flux for 1.6 m/s is 47.1 kW/m^2, compared to 46.8 kW/m^2 using the conduction loss determined from the experimentally measured substrate temperatures.

Table 4
Summary of the average peak net heat flux, time to peak net heat flux, total heating, and the time for total heating for each flow condition with uncertainties of the mean based on a 95% student t evaluation.

Flow Condition (m/s)	Peak Heat Flux (kW/m^2)	Time to Peak (s)	Total Heating (MJ/m^2)	Heating Time (s)
1.6	46.8 ± 5.1	1.5 ± 0.2	1.59 ± 0.17	462 ± 47
1.0	46.1 ± 6.2	1.5 ± 0.3	1.35 ± 0.25	361 ± 70
0.6	48.4 ± 3.7	1.5 ± 0.3	0.99 ± 0.06	311 ± 23
0.05	40.5 ± 7.2	2.0 ± 0.3	0.99 ± 0.03	344 ± 17

There is only 0.6% difference between these two values. For the other flow conditions, the peak net heat flux is also nearly the same regardless of the method used to calculate the conduction loss term. The largest variation is observed for the 0.05 m/s condition, where the net heat flux using semi-infinite analysis for conduction loss was 1.4% higher. Overall, there is an average of 0.9% difference between the peak net heat fluxes using the two different conduction calculations. For the peak net heat flux, it would be acceptable to use either approach for conduction.

The total energy transferred by heat from the firebrand to the TSC during the experiment can be calculated by numerically integrating the net heat flux profile over time. To fully capture the total heating from the firebrand to the TSC, we only consider the times when the net heat flux is positive and in the direction of interest. Other researchers in the literature have quantified the total heating based on water-cooled heat flux gauges measurements, also called "total energy supplied" and "net heat", with values reported for individual cylindrical-shaped firebrands [14] similar to those reported in Table 4. The total heating values in Table 4 show an increase with increasing flow condition. However, accounting for the uncertainty in the mean values over replicates of tests, there is overlap between the total heating for the 1.6 m/s and 1.0 m/s flow conditions and between the total heating for the 0.6 m/s and 0.05 m/s flow conditions. A similar increase in the peak TSC temperatures between the lower flow conditions and the higher flow conditions was noted in Section 3.1.

In the context of total heating, it would be inappropriate to use the net heat flux determined using the semi-infinite analysis for conduction losses. The total heating is determined over longer time scales, between 245 s and 500 s. At these time scales, the semi-infinite analysis underpredicts the conduction heat loss, and the conduction loss has a high relative contribution to the total heat flux. Combined, these factors would underestimate the total heat transferred from the firebrand if the semi-infinite analysis was used. For the 1.6 m/s flow condition, the total heating using semi-infinite analysis for conduction loss is 0.82 MJ/m^2, about half of the total heating calculated using the embedded thermocouple approach. On average for all flow conditions, the semi-infinite approach for the conduction loss leads to total heating values 44% lower than the embedded thermocouple approach.

The increase in total heating with increasing flow condition applies also to the duration of heating (refer to Table 4). For the induced flow cases, as the flow velocity increases, heating occurs over a longer time period. To understand these differences in the duration of total heating over the course of a test, we need to consider the exothermic reactions occurring in the firebrand. The firebrands in these experiments are in a smoldering state. Smoldering combustion is a solid phase oxidation process, where the solid char reacts with oxygen to produce heat, ash, and other combustion products [11]. At higher flow velocities, we hypothesize that oxygen is able to penetrate readily into the smoldering firebrand, either through the ash layer or by blowing away the ash, lengthening the time to sustain smoldering combustion. This would lead to longer heat release from the exothermic char oxidation. As time progresses, a combination of ash layer growth and increased convective, radiative, and conductive losses from the firebrand leads to cooling of the firebrand and a decrease/cessation in the heat transfer from the firebrand to the TSC. For the lower flow conditions, the firebrand cools off more quickly, and there is less total heat transferred to the substrate.

To further support this hypothesis about the connection between air flow velocity and total heating/heating duration, we consider the relationship between the burning rate in the exothermic reactions, mass loss, and air velocity. The mass loss over the duration of burning is a direct indicator of the burning rate. The firebrand mass measurements, taken before generation and after testing, show an increase in mass loss with an increase in flow velocity. The residual mass for the 1.6 m/s flow cases was approximately 67% of the residual mass for the 0.05 m/s cases. Similarly, Lattimer et al. [21] found that the firebrand mass loss rate, which was reported for times greater than 2 s after the start of testing, increased with wind speed. While lengthening the heating duration increases the total heat transferred from the firebrand, the peak heat flux is less correlated with flow velocity. It is more likely that the net heat flux is limited by the wood material and geometry in these experiments, rather than the flow speeds.

4. Conclusions

Improved understanding of the thermal hazard from firebrand deposition is needed to quantify, predict and mitigate the ignition threat posed by firebrands. This study demonstrates the use of a minimally-invasive method to conduct time-resolved measurements of the net heat flux from individual firebrands to a substrate under a range of flow conditions. The net heat flux is obtained through an energy balance on a copper thin skin calorimeter, which is embedded in the substrate and is the same diameter as the deposited firebrand. The net heat flux is the sum of the thermal storage in the TSC and the heat conduction losses to the substrate. The peak net heat flux for the individual disc-shaped birch firebrands is 45 kW/m^2 on average, with no significant differences for different flow conditions. The range of net heat flux measurements is higher than previously reported area-averaged values for individual rod-shaped oak firebrands measured with inverse heat transfer and individual cylindrical birch firebrands measured with a water-cooled heat flux gauge. Increasing flow velocity results in an increase in the peak TSC temperature, firebrand total heating, duration of heating, and total mass consumed, due to the increased accessibility of oxygen. While ignition from firebrands is generally thought to occur from multiple firebrands, these individual firebrands measurements are an important step toward fundamental understanding of firebrand ignition and demonstrate the potential of the TSC measurement technique to study how additional parameters affect the thermal hazard of firebrands. Future work will explore firebrand wood type, moisture content, firebrand size, substrate material, and multiple firebrand interactions.

Declaration of competing interest

The authors declare that they have no known competing financial interests or personal relationships that could have appeared to influence the work reported in this paper.

Data availability

Data will be made available on request

References

[1] V. Radeloff, D. Helmers, H. Kramer, M. Mockrin, P. Alexandre, A. Bar-Massada, V. Butsic, T. Hawbaker, S. Martinuzzi, A. Syphard, S. Stewart, Rapid growth of the US wildland-urban interface raises wildfire risk, Proc. Natl. Acad. Sci. 115 (13) (2018) 3314–3319.

[2] NFPA, Largest loss wildland fires, 2023, National Fire Protection Association, 1 Batterymarch Park, Quincy, MA, https://Www.Nfpa.Org/News-and-Research/Data-Research-and-Tools/Wildland-Urban-Interface/Wildland-Urban-Interface/Largest-Loss-Wildland-Fires. (Accessed 12 January 2023).

[3] Y. Valachovic, Workshop Session, Part 1, Case Study on The Camp Wildfire, Butte County, CA (2018), 2022, University of Maryland - NFPA Fire & Life Safety Ecosystem Symposium, College Park, MD.
[4] S.G. Badger, Large-loss fires and explosions in the United States in 2020, 2021, National Fire Protection Association, 1 Batterymarch Park, Quincy, MA, https://Www.Nfpa.Org/News-and-Research/Data-Research-and-Tools/US-Fire-Problem/Large-Loss-Fires-in-the-United-States.
[5] Insurance Information Institute, Facts + Statistics: Wildfires, 2022, https://Www.Iii.Org/Fact-Statistic/Facts-Statistics-Wildfires. (Accessed 30 November 2022).
[6] B. Teague, S. Pascoe, R. McLeod, The 2009 Victorian Bushfires Royal Commission Final Report, 2010, https://apo.org.au/node/22187.
[7] B. Motal, J.G. Freire, M. Oliveira, S.A. Nunes, R. Dilão, C.C. DaCamara, Using cellular automata to assess the role played by wind direction in two large fire episodes in Portugal, in: D. Viegas, L. Ribeiro (Eds.), Advances in Forest Fire Research 2022, November 2022, p. 431.
[8] The Insurance Institute for Business and Home Safety (IBHS) News Release, Rapid growth of the US wildland-urban interface raises wildfire risk, 2023, Insurance Institute for Business and Home Safety (IBHS), Richburg, SC, March 2019, https://Ibhs.Org/Ibhs-News-Releases/Embers-Cause-Up-To-90-of-Home-Business-Ignitions-During-Wildfire-Events/. (Accessed 5 January 2023).
[9] V. Babrauskas, Ignition Handbook, Fire Science Publishers, Issaquah, WA, 2014.
[10] S. Nazare, I. Leventon, R. Davis, Ignitibility of Structural Wood Products Exposed to Embers During Wildland Fires: A Review of Literature, NIST Technical Note TN 2153, National Institute of Standards and Technology, Gaithersburg, MD, April 2021.
[11] G. Rein, Smoldering combustion, in: SFPE Handbook of Fire Protection Engineering, Springer, 2016, pp. 581–603.
[12] T.J. Ohlemiller, K.M. Villa, Material Flammability Test Assessment for Space Station Freedom, NIST Internal Report IR 4591, National Institute of Standards and Technology, Gaithersburg, MD, June 1991.
[13] S.L. Manzello, T.G. Cleary, J.R. Shields, J.C. Yang, On the ignition of fuel beds by firebrands, Fire Mater. 30 (1) (2006) 77–87.
[14] R.S. Hakes, H. Salehizadeh, M.J. Weston-Dawkes, M.J. Gollner, Thermal characterization of firebrand piles, Fire Saf. J. 104 (2019) 34–42.
[15] F. Richter, B. Bathras, J. Barbetta Duarte, M.J. Gollner, The propensity of wooden crevices to smoldering ignition by firebrands, Fire Technol. (2022) 1–22.
[16] J.C. Thomas, E.V. Mueller, R.M. Hadden, Estimating net heat flux from surrogate firebrand accumulations using an inverse heat transfer approach, in: D.X. Viegas (Ed.), Advances in Forest Fire Research 2018, November 2018, p. 769.
[17] E.D. Bearinger, J.L. Hodges, F. Yang, C.M. Rippe, B.Y. Lattimer, Localized heat transfer from firebrands to surfaces, Fire Saf. J. 120 (2021) 103037.
[18] J.P. Hidalgo, C. Maluk, A. Cowlard, C. Abecassis-Empis, M. Krajcovic, J.L. Torero, A Thin Skin Calorimeter (TSC) for quantifying irradiation during large-scale fire testing, Int. J. Therm. Sci. 112 (2017) 383–394.
[19] H.S. Carslaw, J.C. Jaeger, Conduction of Heat in Solids, Clarendon P Oxford, United Kingdom, 1959.
[20] Z. Tao, B. Bathras, B. Kwon, B. Biallas, M.J. Gollner, R. Yang, Effect of firebrand size and geometry on heating from a smoldering pile under wind, Fire Saf. J. 120 (2021) 103031, Fire Safety Science: Proceedings of the 13th International Symposium.
[21] B.Y. Lattimer, E. Bearinger, S. Wong, J.L. Hodges, Evaluation of models and important parameters for firebrand burning, Combust. Flame 235 (2022) 111619.